

First-principles approach to electric polarization and dielectric constant calculations using generalized Wannier functions

Paweł Lenarczyk* and Mathieu Luisier

Integrated Systems Laboratory, ETH Zürich, 8092 Zürich, Switzerland

(Dated: October 22, 2019)

We describe a method to calculate the electronic properties of an insulator under an applied electric field. It is based on the minimization of an electric enthalpy functional with respect to the orbitals, which behave as Wannier functions under crystal translations, but are not necessarily orthogonal. This paper extends the approach of Nunes and Vanderbilt (NV) [Phys. Rev. Lett. **73**, 712 (1994)], who demonstrated that a Wannier function representation can be used to study insulating crystals in the presence of a finite electric field. According to a study by Fernández *et al.* [Phys. Rev. B. **58**, R7480 (1998)], first-principles implementations of the NV approach suffer from the impact of the localization constraint on the orthogonal wave functions, what affects the accuracy of the physical results. We show that because non-orthogonal generalized Wannier functions can be more localized than their orthogonal counterparts, the error due to localization constraints is reduced, thus improving the accuracy of the calculated physical quantities.

PACS numbers: 71.15.-m, 77.22.Ch, 77.22.Ej

I. INTRODUCTION

The ability to perform first-principles calculations of solids under the influence of finite electric fields is of fundamental as well as practical interest. Linear and nonlinear susceptibilities of materials could be simultaneously extracted from such calculations to determine their dielectric and ferroelectric behavior. These parameters can be further used, for example, in the simulation of electronic devices¹.

At this point the study of materials in a finite electric field remains a challenging theoretical problem². The main difficulty comes from the scalar potential “ $\mathcal{E} \cdot \mathbf{r}$ ” that accounts for the electric field \mathcal{E} . It induces a linear term in the spatial coordinates \mathbf{r} and thus violates the periodicity condition underlying Bloch’s theorem. This term acts as a singular perturbation to the electronic eigenstates. As a consequence, standard computational methods relying on the solution of the eigenfunctions of the effective one-electron Hamiltonian are not suitable for this kind of applications.

This restriction can be alleviated by making use of linear-response theory³, which provides a framework for computing derivatives of various quantities with respect to the applied field. Practically, however, with such techniques only the response to infinitesimal electric fields can be accurately studied. Moreover, their extension to non-linear order is not straightforward and must be carefully handled to avoid divergences in the static limit⁴.

In Ref. 5, Nunes and Vanderbilt (NV) proposed an approach to circumvent the difficulties associated with finite electric fields. They showed that a real-space Wannier function representation could be used to describe an insulating periodic system in the presence of a finite electric field. In this scheme, an electronic enthalpy functional W is minimized with respect to localized orthogonal orbitals. The functional W is made of the usual band-structure energy E_{bs} and a field coupling term $-\mathbf{P}_{el} \cdot \mathcal{E}$.

Here E_{bs} and the macroscopic electronic polarization \mathbf{P}_{el} are expressed in terms of Wannier functions (WFs), the latter via the modern theory of polarization⁶. The NV approach was implemented within density functional theory by Fernández *et al.*⁷, but was hindered by convergence problems with respect to the size of the localization regions of the truncated WFs.

In this paper, we propose an original formalism to perform first-principles calculations of insulators under finite electric fields using non-orthogonal generalized Wannier functions (NGWFs). This extension is motivated by the fact that non-orthogonal wave functions can be considerably more localized than orthogonal ones⁸. Non-orthogonal orbitals have been used in previous computational studies^{9–11} at zero electric field. In this case, they are not truly localized, but rather represent Bloch functions of the cell or supercell calculated at a momentum $\mathbf{k} = 0$. Hence they cannot be applied to finite field situations. Instead, we employ here the orbitals that are truly localized in the manner of Wannier functions and explore the effect of non-orthogonality also in the finite field case. This is done through the implementation of a self-consistent scheme based on the minimization of the electronic enthalpy functional expressed in terms of NGWFs. The resulting solver is then utilized to study the ability of NGWFs to predict the electronic and dielectric properties of materials from first-principles and to discuss the convergence of these physical quantities with respect to the size of the orbital localization region.

The reminder of this paper is organized as follows. In the next section the formalism is presented and its theoretical foundations are introduced. Details about the implementation are given in Sec. III, including a discussion of the minimization procedure and a description of the calculations in real-space. In Sec. IV, we show tests that have been performed to probe the practical usefulness of the method and compare the calculation results using localized wave functions with and without the or-

thogonality constraint. Finally, in Sec. V we conclude and mention possible future developments.

II. FORMALISM

In this work, the pseudopotential approximation¹² to the Kohn-Sham density functional theory¹³ (DFT) is employed. In this context, the problem of interacting electrons and ions is mapped onto a problem of an effective system of N non-interacting valence electrons following the potential of ions screened by the core electrons. The effective Hamiltonian in real-space is equal to

$$H[\rho](\mathbf{r}) = -\frac{1}{2}\nabla^2 + V_{ion}(\mathbf{r}) + V_H[\rho](\mathbf{r}) + V_{xc}[\rho](\mathbf{r}) . \quad (1)$$

Here, the notation $H[\rho](\mathbf{r})$ indicates that the Hamiltonian H is a functional of the electron density $\rho(\mathbf{r})$ and a function of the spatial coordinate \mathbf{r} . Expressed in the same form, V_{ion} is the ion core pseudopotential, V_H the Hartree potential, and V_{xc} the exchange-correlation potential. In this work, the local density approximation (LDA) is adopted and $V_{xc}[\rho](\mathbf{r})$ is derived from the value of the charge density, i.e. $V_{xc}[\rho](\mathbf{r}) = V_{xc}(\rho(\mathbf{r}))$. Atomic units $\bar{e} = \hbar = m_e = 1$ are used throughout the paper.

Within DFT, the total energy of a system of interacting electrons and ions is a unique functional of the electron density $\rho(\mathbf{r})$ and can be written as

$$E[\rho] = E_{bs}[\rho] - E_{dc}[\rho] + E_{II} , \quad (2)$$

where E_{bs} is the band-structure energy that is defined as a trace of the Hamiltonian in the occupied space, $E_{dc} = \int \rho(\mathbf{r}) \left(\frac{1}{2}V_H(\mathbf{r}) + V_{xc}(\rho(\mathbf{r})) - \epsilon_{xc}(\rho(\mathbf{r})) \right) d^3\mathbf{r}$ accounts for double counting in the Coulomb electronic repulsion and for the exchange-correlation corrections, while E_{II} is the Coulomb interaction energy between the ions. By applying the variational principle of Hohenberg and Kohn¹⁴, the ground state energy of the system can be obtained. This requires minimizing the total energy functional E in Eq. (2) with respect to either single particle wave functions¹⁵ or density matrices¹⁰.

In the density matrix description, the expectation value of any operator \hat{O} is given by $\text{tr}[\hat{O}\hat{\rho}]$, where $\hat{\rho}$ is the density matrix operator defined as the projection onto the occupied space. The diagonal element of the density matrix in a spatial representation corresponds to the charge density $\rho(\mathbf{r}) = 2 \langle \mathbf{r} | \hat{\rho} | \mathbf{r} \rangle$, where the factor of 2 accounts for the spin degeneracy. In this formalism the band-structure energy is given by

$$E_{bs}[\rho] = 2\text{tr} \left[\hat{\rho} \hat{H} \right] . \quad (3)$$

In Eq. (3), \hat{H} is the Hamiltonian operator, in the position representation given by Eq. (1). Minimizing Eq. (3) for a fixed, density-independent Hamiltonian and finding a self-consistent solution for the charge density is equivalent to solving the non-linear Kohn-Sham equations¹⁵.

Our goal is to perform the calculations at finite electric fields. The Hamiltonian then becomes

$$H[\rho](\mathcal{E}; \mathbf{r}) = H[\rho](\mathbf{r}) + \mathcal{E} \cdot \mathbf{r} . \quad (4)$$

It has now a parametric dependence on the electric field \mathcal{E} . Replacing $H[\rho](\mathbf{r})$ by $H[\rho](\mathcal{E}; \mathbf{r})$ in Eq. (3) leads to the electronic enthalpy functional

$$W[\rho](\mathcal{E}) = E_{bs}[\rho] - \Omega \mathcal{E} \cdot \mathbf{P}_{el}[\rho] , \quad (5)$$

whose minimization with respect to a set of field-dependent density matrices $\hat{\rho}(\mathcal{E})$ results in the electronic ground state of an insulator in the presence of an electric field. The variable $\mathbf{P}_{el}[\rho]$ refers to the electronic macroscopic polarization. In the density matrix formalism, it is defined as

$$\mathbf{P}_{el}[\rho] = -\frac{2}{\Omega} \text{tr} [\hat{\rho} \hat{\mathbf{r}}] , \quad (6)$$

where $\hat{\mathbf{r}}$ is the position operator and Ω is the volume of the chosen unit cell.

For an insulating crystal, the density operator $\hat{\rho}$ may be expanded in terms of localized functions $\{\nu_a^i\}$, represented below in Dirac's bra-ket notation, as¹⁶

$$\hat{\rho} = \sum_{\substack{ij \\ ab}} |\nu_a^i\rangle K_{ab}^{ij} \langle \nu_b^j| . \quad (7)$$

The upper-case sum over i, j runs over cell replicas whereas the lower-case sum over a, b goes over occupied bands. The periodicity of the crystal is taken into account by imposing that any wave function is obtained by translating that of a reference unit cell, denoted by index 0, with the help of Bravais lattice vectors

$$|\nu_a^i\rangle = \hat{T}_{\mathbf{R}_i} |\nu_a^0\rangle , \quad (8)$$

where $\hat{T}_{\mathbf{R}_i}$ is the translation operator corresponding to the lattice vector \mathbf{R}_i . For the *density kernel* matrix \mathbf{K} the following relation holds¹⁶

$$K_{ab}^{ij} = K_{ab}(\mathbf{R}_j - \mathbf{R}_i) . \quad (9)$$

In the above parametrization of the density operator in Eq. (7), the \mathbf{K} matrix plays the role of an inverse overlap matrix between the generally non-orthogonal $\{\nu_a^i\}$ functions. These functions are called non-orthogonal generalized Wannier functions (NGWFs). Note that for $K_{ab}^{ij} = \delta_{ij} \delta_{ab}$, the wave functions are orthogonal and correspond to the standard Wannier functions (WFs) of a periodic system. For a discussion of the ground state \mathbf{K} matrix properties see Appendix A.

It should be emphasized that similar parametrizations of the density matrix in terms of non-orthogonal orbitals as in Eq. (7) were proposed and used by a number of other authors^{10,11,17,18}. However, in all these studies, the sum over periodic replicas was dropped and the calculations were performed at the Γ -point only, i.e. $\mathbf{k} = 0$.

The wave functions employed in these investigations are in fact extended Bloch functions of the solid. They cannot be directly used to study the response of a periodic system to an electric field because of ill-posedness of the position operator $\hat{\mathbf{r}}$ in the Bloch representation, as explained in Appendix B.

As next step, Eq. (7) is taken as an ansatz for a *trial* density operator and the *physical* density operator

$$\hat{\rho}' = 2\hat{\rho} - \hat{\rho}^2 \quad (10)$$

is introduced. The above *purifying* transformation¹⁹ ensures that $\hat{\rho}'$ does not have eigenvalues larger than 1. This condition on the eigenvalues is termed *weak idempotency*. It is critical to give the underlying energy functional the desired minimal properties²⁰.

In the chosen formalism the expectation value of any operator \hat{O} is re-expressed as $\text{tr}[\hat{\rho}'\hat{O}]$. Thus, the band-structure energy and the electronic polarization per unit cell become

$$E_{bs} = 2 \sum_{i,ab} Q_{ab}^{0i} \langle \nu_a^0 | \hat{H} | \nu_b^i \rangle \quad (11)$$

and

$$\mathbf{P}_{el} = -\frac{2}{\Omega} \sum_{i,ab} Q_{ab}^{0i} \langle \nu_a^0 | \hat{\mathbf{r}} | \nu_b^i \rangle, \quad (12)$$

where

$$Q_{ab}^{ij} = 2K_{ab}^{ij} - (\mathbf{K} \times \mathbf{S} \times \mathbf{K})_{ab}^{ij} \quad (13)$$

and \mathbf{S} is the overlap matrix between the orbitals

$$S_{ab}^{ij} = \langle \nu_a^i | \nu_b^j \rangle. \quad (14)$$

In Eq. (13) the short-hand notation

$$(M \times N)_{ab}^{ij} = \sum_c M_{ac}^{ik} N_{cb}^{kj}$$

is introduced to represent matrix-matrix multiplications between overlap-type matrices $M_{ac}^{ij} = M_{ac}(\mathbf{R}_j - \mathbf{R}_i)$.

The charge density is then given by

$$\rho(\mathbf{r}) = 2 \sum_{i,j,ab} \langle \mathbf{r} | \nu_a^i \rangle Q_{ab}^{ij} \langle \nu_b^j | \mathbf{r} \rangle. \quad (15)$$

Substituting Eqs. (11) and (12) into Eq. (5) leads to an expression for the electronic enthalpy per unit cell

$$W = 2 \sum_{i,ab} (2K_{ab}^{0i} - \sum_{j,k,cd} K_{ac}^{0j} \langle \nu_c^j | \nu_d^k \rangle K_{db}^{ki}) \times \langle \nu_a^0 | \hat{H}(\mathcal{E}) | \nu_b^i \rangle, \quad (16)$$

where $\hat{H}(\mathcal{E}) = \hat{H} + \mathcal{E} \cdot \hat{\mathbf{r}}$. We note that for $K_{ab}^{ij} = \delta_{ij}\delta_{ab}$ the functional in Eq. (16) corresponds to the one originally proposed by NV, which is minimized by orthogonal

orbitals. The introduction of the \mathbf{K} matrix in our approach gives more variational freedom for the minimization and results in non-orthogonal orbitals that can be made more localized, as it will be shown in the following.

The electronic degrees of freedom are the coefficients of the wave functions $\{\nu_a^0\}$ and the density kernel matrix elements $\{K_{ab}^{0i}\}$ in the base cell corresponding to $\mathbf{R}_0 = 0$. The remaining variables are obtained by employing the periodicity relations in Eqs. (8) and (9) for the wave functions and density kernel matrix elements, respectively. Using these conditions, the extremized functional in Eq. (16) can be written explicitly in terms of minimization variables as

$$W = 2 \sum_{i,ab} (2K_{ab}^{0i} - \sum_{j,k,cd} K_{ac}^{0j} \langle \nu_c^0 | \nu_d^{k-j} \rangle K_{db}^{0i-k}) \times \langle \nu_a^0 | \hat{H}(\mathcal{E}) | \nu_b^0 \rangle. \quad (17)$$

The search for the minimum of the functional W requires the knowledge of its partial derivatives with respect to the variational degrees of freedom. In the above Eq. (17), the partial derivatives of W with respect to the minimization variables $\{\nu_a^0\}$ and $\{K_{ab}^{0i}\}$ can be carried out. Differentiating Eq. (17) with respect to ν_a^0 gives:

$$\frac{\partial W}{\partial \nu_a^0} = 4 \sum_{i,b} \left[\hat{H}(\mathcal{E}) | \nu_b^i \rangle Q_{ab}^{0i} + - | \nu_b^i \rangle (\mathbf{K} \times \mathbf{H}(\mathcal{E}) \times \mathbf{K})_{ab}^{0i} \right]. \quad (18)$$

The partial derivative of W with respect to K_{ab}^{0i} has the following form:

$$\frac{\partial W}{\partial K_{ab}^{0i}} = 2 \left[2H_{ab}^{0i} - (\mathbf{H}(\mathcal{E}) \times \mathbf{K} \times \mathbf{S})_{ab}^{0i} + - (\mathbf{S} \times \mathbf{K} \times \mathbf{H}(\mathcal{E}))_{ab}^{0i} \right] \quad (19)$$

Above, $\mathbf{H}(\mathcal{E})$ stands for the matrix representation of the Hamiltonian $H_{ab}^{ij} = \langle \nu_a^i | \hat{H} | \nu_b^j \rangle$ in the basis of the employed localized orbitals, WFs or NGWFs.

III. COMPUTATIONAL DETAILS

We now give a brief description of our implementation of the formalism presented above. It was integrated into PARSEC²¹ open-source DFT code. The modified package was used to obtain the results reported in the following section.

The wave functions $\{\nu_a^0\}$ are represented on a uniform real-space grid with spacing h in each direction. Since these functions are required to be spatially localized, they have non-zero values only on the grid points inside the localization regions (LRs). In the present work, we let each LR be a cube of edge size a_{LR} . The centers of the

LRs may be chosen arbitrarily. For the cutoff of the density kernel matrix, the K_{ab}^{0i} elements are non-zero only if the LR of v_a^0 and v_b^i overlap. Note that if this localization condition is imposed, the sums over periodic replicas (i,j,k,l) appearing in the preceding section become finite. They are determined by the set of LR that overlap with all LR centered in the supercell containing the origin and indicated by the index 0.

By using a homogeneous grid, the real-space integration is replaced by a summation over the discretization points, so that, e.g., the overlap matrix elements can be calculated as

$$S_{ab}^{ij} \simeq h^3 \sum_{\mathbf{r}_g} v_a^i(\mathbf{r}_g) v_b^j(\mathbf{r}_g) .$$

The sum goes over the set of grid points \mathbf{r}_g that are shared by the localization regions of both v_a^i and v_b^j orbitals. Note that h^3 is the volume of each grid point.

The Hamiltonian operator is evaluated directly on the real-space grid, as implemented in the PARSEC code²². A finite-difference expansion of order M of the Laplacian ∇^2 is used to evaluate the kinetic energy operator. The ionic potential V_{ion} is determined by a pseudopotential cast in the Kleinman-Bylander form²³. The Hartree and exchange-correlation potentials $V_H(\mathbf{r})$ and $V_{xc}(\mathbf{r})$ are represented by numerical values on the grid. The real-space Hamiltonian $H(\mathbf{r})$ in PARSEC is defined only in the base supercell. To act on the localized orbitals $\{v_a^i\}$ the Hamiltonian is circularly shifted to the LR of the orbitals and evaluated there.

In the tests presented below, we use norm-conserving pseudopotentials generated with the method of Troullier and Martins¹² and obtained from Ref. 21. The exchange and correlation effects are treated within the local-density functional of Ceperley and Alder²⁴, as parameterized by Perdew and Zunger²⁵.

The evaluation of the Hamiltonian and two-center integrals allows one to calculate the enthalpy functional W in Eq. (17) and its derivatives $\frac{\partial W}{\partial v_a^0}$ and $\frac{\partial W}{\partial K_{ab}^{0i}}$ in Eqs. (18) and (19), respectively. It enables a search for the ground state that minimizes the energy. This optimization can be carried out in two nested stages

$$W_{min} = \min_{\{v_a^0\}} W'(\{v_a^0\}) , \quad (20)$$

with

$$W'(\{v_a^0\}) = \min_{\{K_{ab}^{0i}\}} W(\{K_{ab}^{0i}\}, \{v_a^0\}) . \quad (21)$$

The minimization with respect to the density kernel in Eq. (21) ensures that W' of Eq. (20) is a function of NGWFs only. The above minimizations has been implemented with a conjugate gradient scheme based on the analytical gradients from Eq. (18) to optimize the orbitals in Eq. (20) and from Eq. (19) for the optimization of the density kernel in Eq. (21). The gradients are made mutually conjugate using Polak-Ribière formula²⁶. The nested

minimization approach is inspired by the method developed in Ref. 27 in the context of zero field calculations with periodic non-orthogonal wave functions. When optimizing WFs we set the density kernel to an identity matrix $K_{ab}^{0i} = \delta_{0i} \delta_{ab}$ and skip the minimization in Eq. (21). This results in the orthogonal wave functions as shown in Appendix A.

During the electronic enthalpy minimization, as described above, the Hamiltonian is kept fixed. This has the practical advantage that the enthalpy functional in Eq. (17) is a quartic function of the $\{v_a^0\}$ coefficients and a quadratic function of the $\{K_{ab}^{0i}\}$ elements. The conjugate-gradient line searches can therefore be solved exactly²⁸ by computing the coefficients of the fourth and second-order polynomials for the orbital and density kernel optimizations, respectively. In order to assure the existence of a minimum, the Hamiltonian eigenspectrum is shifted by a transformation $H \rightarrow H - \mu I$, where μ is a free parameter that makes all the eigenvalues negative. A discussion of this transformation and its impact on the minimized enthalpy functional is deferred to Appendix A.

The results of the minimization algorithm are the grid coefficients $\{v_a^0(\mathbf{r}_g)\}$ of the wave functions in the base cell and the corresponding matrix elements $\{K_{ab}^{0i}\}$. The functions $\{v_a^i\}$ and the elements $\{K_{ab}^{ij}\}$ are evaluated on-the-fly when calculating the sums over the replicas (i,j,k,l) . The periodicity relations of the wave functions in Eq. (8) and of the matrix elements in Eq. (9) are exploited to do that. The charge density $\rho(\mathbf{r})$ is periodic in the supercell and is calculated according to Eq. (15). At the end of the minimization procedure, if it is found that the charge density as well as the Hartree and exchange-correlation potentials are not consistent, the whole operation is repeated with the updated potentials, as in standard self-consistent field (SCF) cycle.

IV. RESULTS

In this section the application of the above described methodology is presented. In particular, we emphasize that the main purpose of the conducted study is to exhibit and understand the impact of the localization constraint on the accuracy of the ground state and finite-field calculations, using orthogonal and non-orthogonal Wannier functions: WFs and NGWFs respectively.

Since DFT is variational²⁹, any restriction placed on the class of density matrices that can be searched over has the effect of raising the minimum energy E_{bs} Eq. (3) above its true ground state value E_0 . This suggests that the error introduced by using LR of finite size a_{LR} in the minimization Eq. (20) can be assessed by calculating

$$\Delta E_{bs}(a_{LR}) = E_{bs}(a_{LR}) - E_0 , \quad (22)$$

where $E_{bs}(a_{LR})$ is the minimum band-structure energy at a_{LR} and E_0 is the reference energy, with no localization constraints. The value of E_0 can be estimated

by the conventional diagonalization of the Hamiltonian using Bloch functions and converged \mathbf{k} -point sampling.

In general it can be presumed that the density matrix $\rho(\mathbf{r}, \mathbf{r}')$ in the true ground state tends to zero as the separation of its arguments $|\mathbf{r} - \mathbf{r}'|$ increases³⁰. In an early pioneering work, Kohn³¹ proved that the density matrix and Wannier functions for a one-dimensional (1D) model crystal decay exponentially in systems with a band gap. In a more recent work, He and Vanderbilt³² demonstrated that in 1D insulators the spatial decay of the density matrix and Wannier functions has the form of a power law times exponential, what results in a faster decay than that predicted by Kohn. These authors have also shown that for 1D model problems non-orthogonal Wannier-like functions exhibit superior localization as compared to orthogonal ones. In the all three spatial dimensions, the exponential decay of the Wannier functions has been proven for a single-band case³³, and that of the density matrix has been proven in general³⁰. For the density matrix also some simple predictions of the inverse decay length are available, in the tight-binding³⁴, and weak-binding³⁵ limits.

The above considerations strongly suggests that the error in the energy should go quickly to zero with the increase of the real-space cutoff R_C imposed on $\rho(\mathbf{r}, \mathbf{r}')$: $\rho(\mathbf{r}, \mathbf{r}') = 0$, $|\mathbf{r} - \mathbf{r}'| > R_C$. The localization properties of the density matrix create a fundamental basis for the development of various expansion algorithms^{36–41} which enable calculations of density matrix with computational complexity that scale linearly with system size. In our formulation the cutoff R_C is controlled by the size of LR, $\frac{a_{LR}}{2}$, of the localized functions $\{\nu_a^i\}$ and the dimension of the density kernel matrix \mathbf{K} , as can be seen by substituting $\rho(\mathbf{r}, \mathbf{r}') = \langle \mathbf{r} | \hat{\rho} | \mathbf{r}' \rangle$ in the expansion Eq. (7). It will be verified by the test calculations below that the error $\Delta E_{bs}(a_{LR})$ decreases with increasing a_{LR} .

A strict localization is not compatible with orthogonality⁸. This introduces an error in the total particle number, what can be examined by looking at the quantity

$$\Delta N(a_{LR}) = N - \int \rho(a_{LR}; \mathbf{r}) \, d\mathbf{r} , \quad (23)$$

where N is the number of valence electrons in the system, and $\rho(a_{LR}; \mathbf{r})$ denotes the charge density optimized at a_{LR} . Since there are only $\frac{N}{2}$ eigenvalues of $\hat{\rho}$ that are different from 0, and because these eigenvalues are constrained to be smaller or equal to 1, N is a rigorous upper bound to $2\text{tr}\hat{\rho} = \int \rho(\mathbf{r}) \, d\mathbf{r}$ and ΔN is necessarily non-negative as it will be exemplified below.

The electronic response of an insulating solid to applied electric field \mathcal{E} can be quantified by considering high-frequency dielectric constants. The dielectric tensor ϵ is related to the macroscopic polarization \mathbf{P} by

$$\epsilon_{\alpha\beta} = \delta_{\alpha\beta} + 4\pi \frac{dP_\alpha}{d\mathcal{E}_\beta} , \quad (24)$$

where α and β indicate Cartesian coordinates. It can be

obtained by finite differences of the induced polarization vector components P_α for different values of \mathcal{E}_β coefficients. That is, \mathcal{E}_β is increased by small increments $\Delta\mathcal{E}$ and the computed values of P_α are used to evaluate 1-st order approximation: $\frac{dP_\alpha}{d\mathcal{E}_\beta} \approx \frac{P_\alpha(\mathcal{E}_\beta + \Delta\mathcal{E}) - P_\alpha(\mathcal{E}_\beta)}{\Delta\mathcal{E}}$, substituted in Eq. (24). The calculation is repeated for a few values of $\Delta\mathcal{E}$ to minimize the impact of numerical errors. If the ions are kept fixed, as for the results reported below, this gives high-frequency dielectric constants $\epsilon_{\alpha\beta}^\infty$. It will be shown that the calculation of ϵ^∞ converges exponentially as the size of the localization a_{LR} is increased. Fitting the calculated values of ϵ^∞ at different a_{LR} , using the function

$$\epsilon^\infty(a_{LR}) = A \exp(-(a_{LR}/a)/\alpha) + B , \quad (25)$$

allows to extract dielectric constants in the limit of no localization constraint $\epsilon^\infty(a_{LR} \rightarrow \infty) = B$.

Two different systems were selected to test the implementation of our method. The first structure — bulk Silicon is chosen due to its practical relevance and because it often serves as a benchmark for DFT codes^{7,9,10}. The second one is cubic BaTiO₃ which has very interesting bonding properties examined so far only using Maximally localized Wannier functions¹⁶ (MLWFs), constructed from Bloch orbitals at zero electric field⁴².

A. Bulk Silicon

The simulation of bulk Silicon is performed using periodically continued cubic cell containing 8 atoms arranged in a diamond structure. The lattice parameter used is $a = 10.2 \, a_0$, a_0 denoting the atomic length unit. A total of $N = 32$ valence electrons are accounted for by 16 doubly occupied orbitals. The LR of the considered orbitals are centered on the bonds connecting one Si atom with its four nearest neighbors. Their start values are assumed to be centrosymmetric Gaussian functions with their origin at the localization centers and their variance corresponding to half of the Si–Si bond length. The identity matrix is used as a initial guess for \mathbf{K} . The converged grid spacing is $h = 0.3 \, a_0$ and we employ $M = 6$ order finite difference expansion for the Laplacian operator. The chemical potential is set to $\mu = 3 \, \text{Ry}$. With these parameters, the minimizations are carried out until the change in the energy is less than $10^{-6} \, \text{Ry/atom}$. For comparison purposes, we also perform calculations using extended Bloch functions with the same real-space setup as for the localized wave functions and $3 \times 3 \times 3$ Monkhorst-Pack grid⁴³ for the computations in reciprocal space.

Fig. 1 shows the error in the band-structure energy from Eq. (22) evaluated for different LR sizes a_{LR} and compared to the reference value resulting from a sum of $\frac{N}{2}$ doubly-occupied Bloch eigenstates over the considered \mathbf{k} -points.

The results displayed in Fig. 1 demonstrate that the effect of non-orthogonality is especially pronounced for

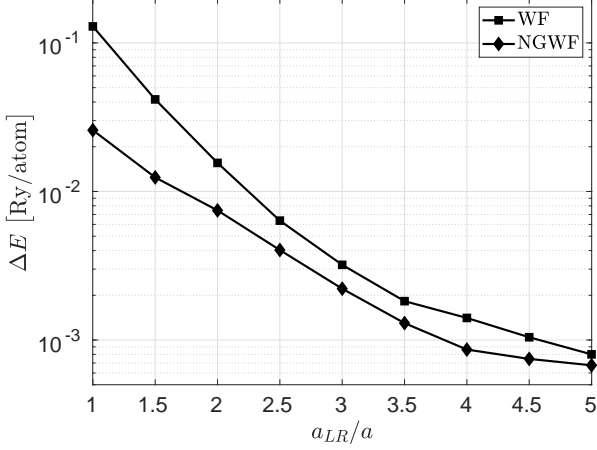


FIG. 1. Si: Error in band-structure energy ΔE_{bs} versus the size a_{LR} of the localization regions. Squares: Wannier functions (WFs). Diamonds: non-orthogonal generalized Wannier functions (NGWFs). a_{LR} is normalized with the lattice constant $a = 10.2a_0$.

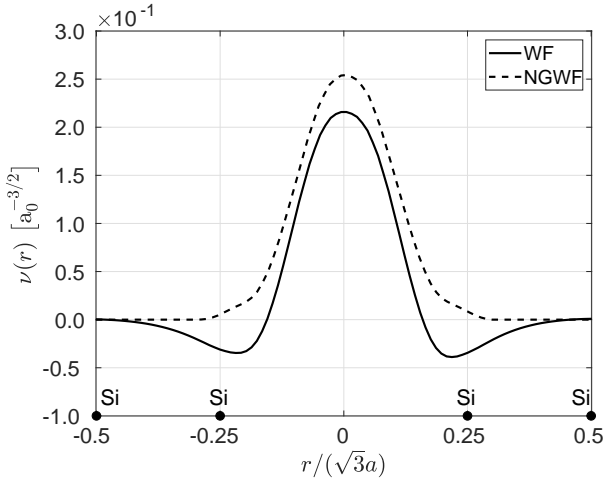


FIG. 2. Si: Line plot of σ -oriented wave functions along Si-Si bond in the ground state. $|r|$ is the distance from the localization center. Solid line: WF. Dashed line: NGWF. The wave functions are constrained to be zero outside the localization region of size $a_{LR} = 2a$.

strict localization constraints: $a_{LR} < 2a$. This improvement can be understood by examining Fig. 2 which plots the profiles of the wave functions along Si-Si bond. As can be observed both WFs and NGWFs are localized, but in the WF case the tail of the wave function does not decay as rapidly as with NGWF. This feature of WF is dictated by the orthogonality requirement. The two roots of $\nu(r)$ in Fig. 2 correspond to the positions where the wave function must be zero in order to be orthogonal to the neighboring orbitals. Consequently, the NGWFs can be made better localized than WFs, because they do not need to fulfill the orthogonality constraints. This

results into a reduction of the energy error ΔE_{bs} when working with non-orthogonal orbitals.

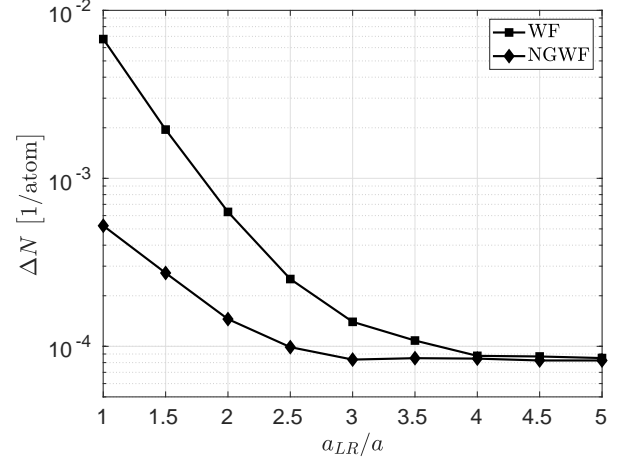


FIG. 3. Si: Error in total particle number ΔN versus localization size a_{LR} . Squares: WFs. Diamonds: NGWFs.

Fig. 2 confirms that strict localization is not compatible with orthogonality. The corresponding error in total particle number from Eq. (23) is plotted in Fig. 3 as a function of the localization size a_{LR} . The results show that the accuracy losses due to the orthogonality constraint in the limit of strong localization can be significantly reduced by using NGWFs instead of WFs. This enhancement can be attributed to the inclusion of the density kernel matrix \mathbf{K} to compensate for the non-orthogonality of the orbitals.

As next step, we address the question of relaxing the orthogonality constraint on the localized wave functions and its influence on the electronic response of bulk silicon to external electric fields. In order to quantify the difference between WFs and NGWFs, the electronic dielectric constant ϵ^∞ has been calculated using Eq. (24) at different a_{LR} . For the considered zinc blende structure it holds $\epsilon = \epsilon_{xx} = \epsilon_{yy} = \epsilon_{zz}$. The electric field used to induce the electronic response is applied along the [100] direction with maximum intensity equal to $\bar{e}|\mathcal{E}| = 10^{-2}\text{Ry}/a_0$. The weak intensity of the field guarantees the linear response of the material and lies well below the onset of the Zener breakdown. The results are shown in Fig. 4.

As can be seen in Fig. 4 the convergence of ϵ^∞ with respect to a_{LR} is exponential. Fitting the data using the function in Eq. (25) gives the limit of the no localization constraint $a_{LR} \rightarrow \infty$. The value of $\epsilon^\infty(a_{LR} \rightarrow \infty)$ is 12.7 for WFs and 12.8 for NGWFs. Fernández *et al.* reported in Ref. 7 a value of 13.4 for analogous calculations using orthogonal Wannier functions. The LRT results of ϵ^∞ vary between 12.6 to 12.9, depending on the details of the calculation⁴⁴. Therefore, it can be concluded that the difference in the extracted values of ϵ^∞ between our results and those of Fernández *et al.* remains within an acceptable range. The convergence of ϵ^∞ with respect

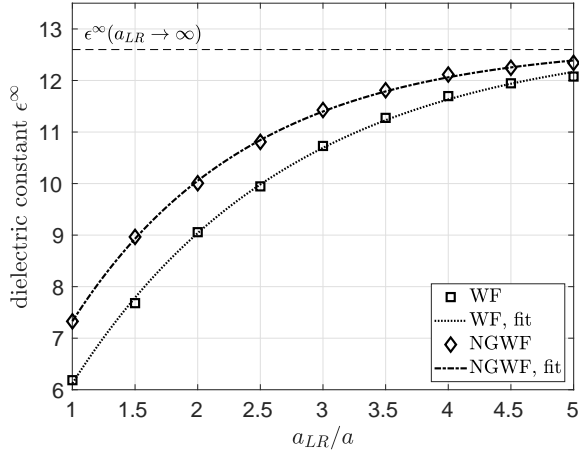


FIG. 4. Si: Electronic dielectric constant ϵ^∞ computed with WFs (squares) and NGWFs (diamonds) for different sizes of the localization regions a_{LR} . The dotted and dash-dotted lines display fittings of Eq. (25) to WF and NGWF data, respectively. The vertical dashed line shows the average of the extrapolated fitted curves in the limit $a_{LR} \rightarrow \infty$.

TABLE I. Si: Fitting parameters of $\epsilon^\infty(a_{LR})$ function in Eq. (25) to the WF and NGWF data in Fig. 4. The values from Ref. 7 are for calculations using orthogonal Wannier functions. The value of α in Ref. 7 is multiplied by a factor of 2 to account for the $a_{LR} \mapsto 2a'_{LR}$ relation between localization region size a_{LR} used in our work and a'_{LR} used in Ref. 7.

Calculation	α	A	B
WF	1.77	-11.9	12.7
NGWF	1.39	-11.0	12.8
Ref. 7	1.62	-13.2	13.4

to a_{LR} was also found to be exponential in Ref. 7 for bulk Si using orthogonal Wannier functions. Note that the definition of localization size in Ref. 7 corresponds to $\frac{1}{2}a_{LR}$ in our work. The fitting parameters of Eq. (24) for WF and NGWF data in Fig. 4 as well as the results from Ref. 7 are given in Table I. As it can be seen our calculation with orthogonal Wannier functions converges slower than that of Fernández *et al.*. As a consequence large LRs are required for reliable estimations of the electronic response. The situation is improved by using non-orthogonal orbitals. If, for example, a convergence to within 5% of $\epsilon^\infty(a_{LR} \rightarrow \infty)$ is acceptable, then a localization region with $a_{LR} = 3.7a$ is needed in the case of NGWFs, $a_{LR} = 4.6a$ for WFs. Hence, the amount of required real-space volume decreases by a factor of 1.9 to represent each wave function.

The significant impact of the localization constraint on the electronic response calculations reported above can be better understood by examining of how the wave functions change under the action of an external electric field. Fig. 5 shows the variation of the wave func-

tions $\Delta\nu(r) = \nu(\mathcal{E}; r) - \nu(r)$ along Si-Si bond due to an electric field $\vec{e}|\mathcal{E}| = 10^{-2}\text{Ry}/a_0$ applied along the [111] direction, parallel to the bond. The field-induced wave functions $\Delta\nu(r)$ are calculated with respect to the ground state ones $\nu(r)$ displayed in Fig. 2. Looking at Figs. 2 and 5 it can be seen that because $\Delta\nu(r) \times \nu(r) \gtrless 0$ for $r \lessgtr 0$, the field-polarized wave functions $\nu(\mathcal{E}; r)$ are amplified at $r < 0$ and damped at $r > 0$. Therefore, the centroids of charge of the orbitals are shifted with respect to the zero-field case. The displacement occurs in the positive direction of the r axis, opposite to the applied field. From Eq. (12) it can be concluded that this gives rise to an induced electronic polarization $\Delta\mathbf{P}_{el}(\mathcal{E}) = \mathbf{P}_{el}(\mathcal{E}) - \mathbf{P}_{el}(0)$, in the direction compatible with the field. It is used to quantify the dielectric response of the material according to Eq. (24). The results in Fig. 5 show that the field-induced wave functions are better constrained within the localization region for non-orthogonal Wannier functions than for orthogonal ones. This lead to (i) a lower impact of the localization constraints when studying the electronic response with NGWFs and (ii) a more reliable value of the dielectric constant calculated for small localization regions.

The ground state and field polarized Wannier functions of Si are shown in Fig. 6. These σ type orbitals are oriented along Si-Si bond. The orbitals are constrained to be zero outside the LRs with size $a_{LR} = 2a$. The polarized orbitals are induced by an electric field $\vec{e}|\mathcal{E}| = 10^{-2}\text{Ry}/a_0$ applied along the bond in [111] direction. It is encouraging to notice the similarity of the ground state WF in Fig. 6a to maximally localized Wannier functions in bulk silicon¹⁶. As is apparent in Fig. 6a the ground state WF orbital represents the intuitive chemical concept of a covalent bond. It clearly

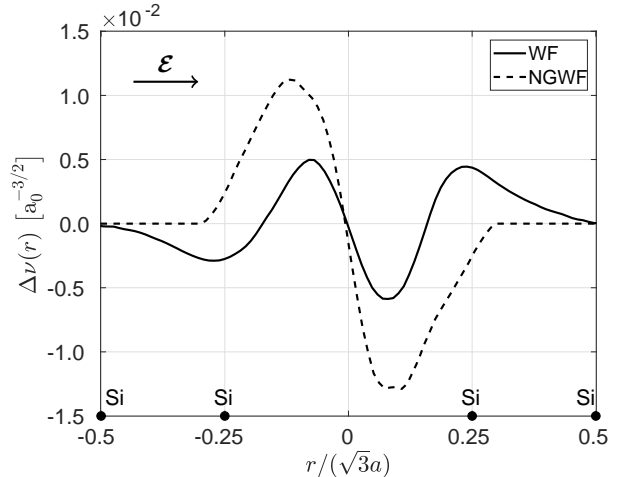


FIG. 5. Si: Variation $\Delta\nu(r) = \nu(\mathcal{E}; r) - \nu(r)$ of σ wave functions along Si-Si bond due to an electric field $\vec{e}|\mathcal{E}| = 10^{-2}\text{Ry}/a_0$ applied in the direction parallel to the bond. Solid line: WF. Dashed line: NGWF. The reference ground state wave functions $\nu(r)$ are displayed in Fig. 2.

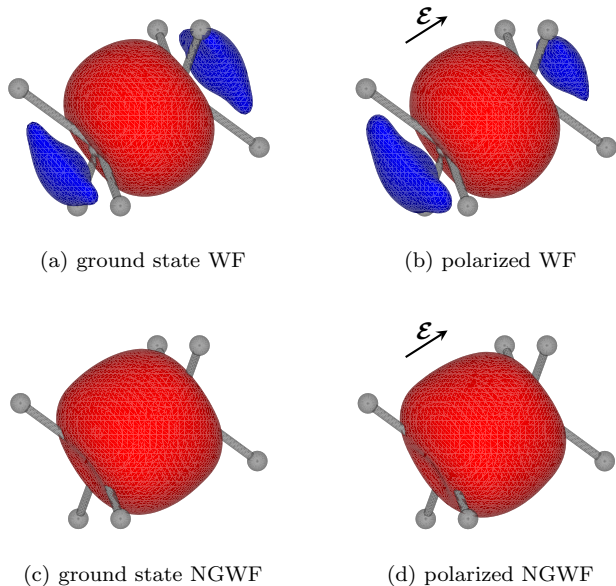


FIG. 6 (Color online). Si: Amplitude isosurface plots of bond-centered σ wave functions at zero electric field (ground state orbitals) and in presence of macroscopic electric field (polarized orbitals). The isosurfaces are taken at $\pm 2 \times 10^{-3} a_0^{-3/2}$ (red and blue surfaces correspond to positive and negative amplitudes, respectively). The two bonded Si atoms are shown (partially covered by the bonding wave function) as well as their three remaining nearest-neighbors. The polarized orbitals are induced by the electric field \mathcal{E} along [111] direction as indicated by arrows. Drawings created with VESTA program⁴⁵.

displays the character of the σ -bonding wave function created by the constructive interference of two sp^3 hybrid atomic orbitals centered on the bonded atoms. In addition, it can be seen in Fig. 6b that this covalent bond and its centroid of charge are shifted in the direction anti-parallel to the applied electric field. The main difference in NGWFs as compared to WFs noticeable in Fig. 6 is the absence of p -like contributions on Si, what makes NGWFs more localized and therefore better suited for practical calculations. The better localization of NGWFs as compared to WFs is more apparent in Fig. 2 which shows the line cuts along rotation symmetry axis of the profiles displayed in Fig. 6a (WF) and Fig. 6c (NGWF).

B. Cubic Barium Titanate

We now turn to a more complex system — BaTiO_3 in the centrosymmetric phase. The simulation structure is a cubic perovskite unit cell. It is composed of a Ba atom placed in the cube corner, a Ti atom sitting at the body-center position, and 3 O atoms occupying the face-centers of the perpendicular sides. The lattice parameter used is $a = 7.7a_0$ (a_0 denotes atomic length unit). The $N = 24$ valence electrons are covered by 12 doubly occupied or-

bitals. We consider localization regions of these orbitals centered on the O atoms and assign 4 localization centers to each of the 3 O atoms. The 4 orbitals in the overlaying localization regions are initialized with Gaussians having a s , px , py and pz symmetry, and origin on the central O atom. A grid spacing of $h = 0.3a_0$ and finite difference discretization order $M = 6$ is used. The chemical potential is set to $\mu = 6\text{Ry}$. The reference energy calculations are performed using a $3 \times 3 \times 3$ Monkhorst-Pack mesh⁴³ for the Brillouin Zone sampling.

Fig. 7 shows the convergence of the band-structure energy of BaTiO_3 with respect to the size of localization a_{LR} . We observe that, similarly to the bulk silicon case (see Fig. 1), allowing the wave functions to be non-orthogonal reduces the error in the calculation due to the localization constraint. We note however a faster convergence in the case of BaTiO_3 than for Si.

The results presented in Fig. 7 are supported by carefully examining the profiles of the orbitals. An exemplary line cut of the σ -type (pz -initialized) orbital along a Ti–O–Ti bond in [001] direction is displayed in Fig. 8. As it can be seen, the non-orthogonal wave function is well contained within a distance $|z| < 2a$. In contrary, the orthogonal one presents a significant amplitude around distant O atoms located at $z = \pm 2a$. A similar behavior was observed for the other types of the orbitals. As a consequence a larger LR is required for orthogonal wave functions than for non-orthogonal ones in order to reduce the impact of the localization constraint on the quality of the calculations.

The error due to incompatible localization and orthogonality constraints manifests itself in the deviation of the total particle number from its nominal valence value expressed by Eq. (23). This can be observed in Fig. 9. As is apparent, in the limit of strong localization, the accuracy

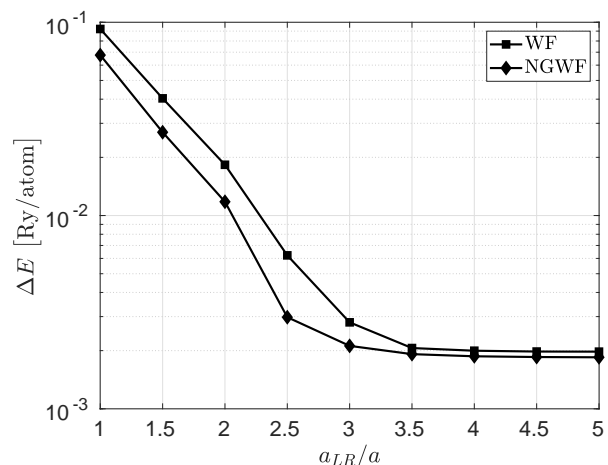


FIG. 7. BaTiO_3 : Error in band-structure energy ΔE_{bs} versus the size a_{LR} of the localization regions. Squares: Wannier functions (WFs). Diamonds: non-orthogonal generalized Wannier functions (NGWFs). a_{LR} is normalized with the lattice constant $a = 7.7a_0$.

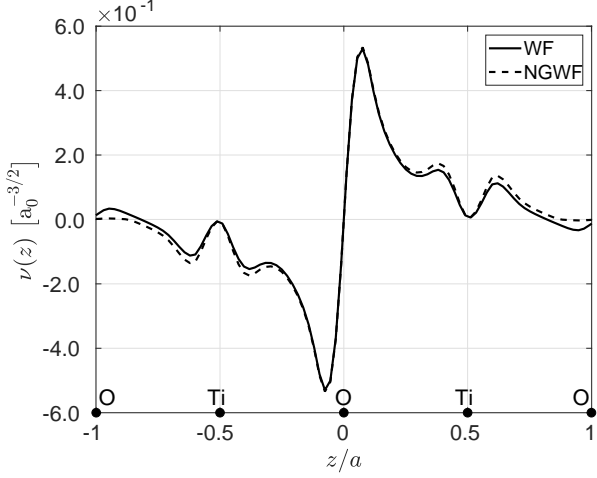


FIG. 8. BaTiO₃: Line plot of Oxygen-centered σ wave functions in ground state. The orbitals are oriented parallel to the Ti–O–Ti bond in the [001] direction. $|z|$ is the distance from the localization center along the [001] axis. Solid line: WF. Dashed line: NGWF. The wave functions are constrained to be zero outside localization region of size $a_{LR} = 3a$.

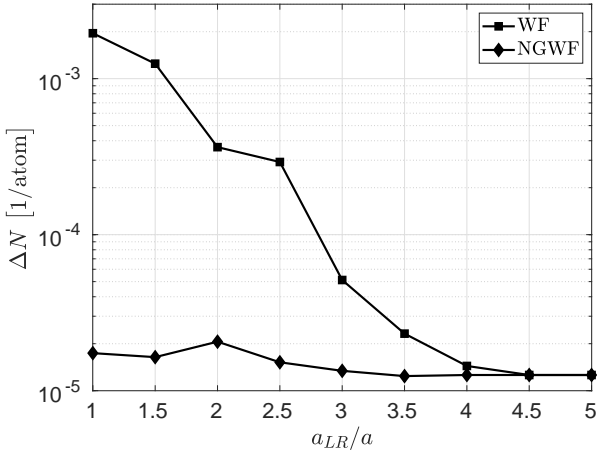


FIG. 9. BaTiO₃: Error in total particle number ΔN versus the localization size a_{LR} . Squares: WFs. Diamonds: NGWFs.

losses are severe when using WFs, but not for NGWFs for which the inclusion of the \mathbf{K} matrix compensates for the non-orthogonality of the wave functions.

Fig. 10 presents the electronic dielectric constant of cubic BaTiO₃ calculated using WFs and NGWFs as a function of localization region size a_{LR} . Due to the inversion symmetry of the considered cubic perovskite structure it holds: $\epsilon = \epsilon_{xx} = \epsilon_{yy} = \epsilon_{zz}$. In the calculations, the electric field is applied along the [001] direction, by varying \mathcal{E}_z coefficient, and the computed values of the induced $P_{el,z}$ polarization component are used to evaluate the ϵ_{zz}^∞ tensor element according to Eq. (24). The maximum intensity of the field is $\bar{e}|\mathcal{E}| = 10^{-2}\text{Ry}/a_0$. As can be seen in

Fig. 10 the computed values of ϵ^∞ converge exponentially with increasing a_{LR} . Fitting the data using the function in Eq. (25) gives in the limit $a_{LR} \rightarrow \infty$ the values of ϵ^∞ equal to 5.77 for WFs and 5.84 for NGWFs. Published LRT results vary between 5.60 and 6.80⁴⁶. The experimental value is 5.4⁴⁷.

As can be seen in Fig. 10 the electronic response of BaTiO₃ is practically converged at a_{LR} equal to $3.8a$ and $2.7a$ when using WFs and NGWFs, respectively. In this case the error in ϵ^∞ is less than 5% of the average extrapolated value ϵ^∞ at $a_{LR} \rightarrow \infty$. This is quite different from the case of Si, which requires LR that contain larger number of unit cells a_{LR}/a to perform the calculations of the same quality. As for Si, by using non-orthogonal orbitals the impact of the localization constraint on the dielectric response is reduced. In the case of BaTiO₃ the volume fraction of LRs giving a relative error in ϵ^∞ of 5% for WFs and NGWFs is 2.6.

To shed light on the charge transfer in BaTiO₃ due to external electric field, we have listed in Table II a decomposition of the induced polarization coming from the individual orbitals. The orbitals are labeled by their dominant atomic character on the O atom at the localization center. The O atoms are classified in two groups: the O atom along the [001] axis, denoted as O_Z, and the O atoms in (001) plane, named O_{XY}. The results listed in table II show that the contributions from the same types of orbitals are similar for WFs and NGWFs. We also note that the form of the decomposition is almost independent from the size of the localization region — the changes in the relative orbitals contributions are less than 1% for $a_{LR} = [1, 5]a$. As it stands out from a further inspection of the table, the O_Z(p_z) orbital gives

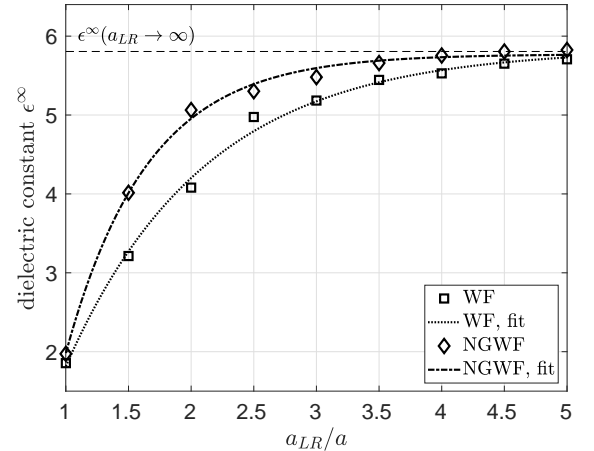


FIG. 10. BaTiO₃: Electronic dielectric constant ϵ^∞ computed with WFs (squares) and NGWFs (diamonds) for different sizes of localization regions a_{LR} , normalized by the lattice constant $a = 7.7a_0$. The dotted and dash-dot lines display fitting of Eq. (25) to WF and NGWF data respectively. The vertical dashed line show the average of the extrapolated fitted curves in the limit of $a_{LR} \rightarrow \infty$.

TABLE II. BaTiO₃: Orbital decomposition of the induced electronic polarization $dP_{el} = P_{el}(\mathcal{E}) - P_{el}(\mathbf{0})$ due to electric field $\bar{e}|\mathcal{E}| = 10^{-2}\text{Ry}/a_0$ along [001] direction for WFs and NGWFs. These values correspond to relative contributions $\frac{dP_{el,i}}{dP_{el}}$ of the individual orbitals $i = 1, \dots, 12$. The equivalent orbitals on the two O_{XY} atoms give the same contributions to dP_{el} .

Atom	Orbital	Calculation	
		WF	NGWF
O _Z	<i>s</i>	0.003	0.002
O _Z	<i>p_x</i>	0.161	0.161
O _Z	<i>p_y</i>	0.161	0.161
O _Z	<i>p_z</i>	0.343	0.344
O _{XY} (×2)	<i>s</i>	0.000	0.000
O _{XY} (×2)	<i>p_x</i>	0.041	0.040
O _{XY} (×2)	<i>p_y</i>	0.022	0.022
O _{XY} (×2)	<i>p_z</i>	0.103	0.104

dominant contribution to the induced polarization, for the electric field applied in [001] direction. This orbital corresponds to the σ wave functions displayed in Fig. 8.

Fig. 11 shows how the σ wave functions of BaTiO₃ change under an applied electric field. As it can be seen, for the orthogonal wave function a large charge transfer is present around distant O atoms located at $z = \pm 2a$. In consequence by using $a_{LR} < 2a$ leads to a significantly reduced electronic response and results in an underestimated value of ϵ^∞ , as reported in Fig. 10. Because non-orthogonal wave functions are only slightly perturbed by the electric field at distances $|z| > 2a$, a better convergence of the dielectric constant calculations is obtained with NGWFs than by using WFs.

Finally, in Fig. IV B we show the isosurfaces of the σ orbitals oriented along Ti–O–Ti bond in [001] direction. They result from p_z atomic orbitals centered on O atom along [001] axis, after minimization of the electric enthalpy functional under the localization constraint $a_{LR} = 3a$. The ground state orbitals correspond to zero field calculation and the polarized orbitals are induced by an electric field $\bar{e}|\mathcal{E}| = 10^{-2}\text{Ry}/a_0$ applied in the [001] direction. We note the similarity of the ground state WF in Fig. 12a to the corresponding MLWF in centrosymmetric Barium Titanate⁴². As it can be seen in Fig. 12a, the wave function show clearly the hybridization between p_z orbital on the O atom in the center and d_{z^2} orbitals on the neighboring Ti atoms. The hybridization to Ti d_{z^2} states appears in the form of tori surrounding the Ti atoms (in Fig. IV B the Ti atoms are embedded in the d_{z^2} orbitals). Such hybridization is at the origin of the ferroelectric instability as argued by Posternak *et al.*⁴⁸.

The application of the electric field changes the chemical bonding, as indicated in Fig. IV B. For the electric field acting in the [001] direction, the hybridization weakens for the upper O–Ti bond and strengthens for the lower one, endowing the wave functions with less d_{z^2}

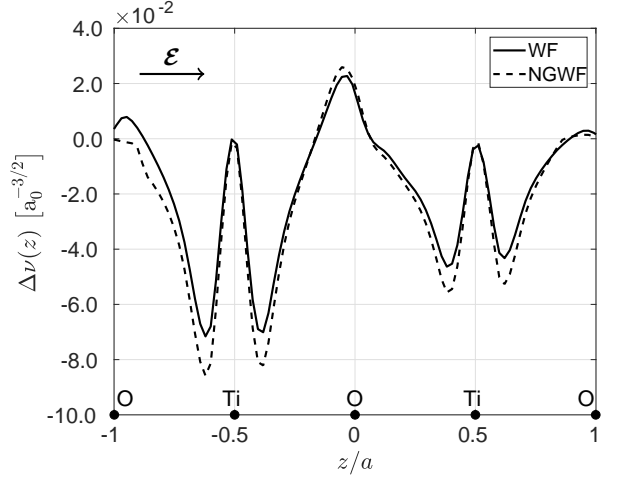


FIG. 11. BaTiO₃: Variation $\Delta\nu(z) = \nu(\mathcal{E}; z) - \nu(z)$ of σ wave functions along Ti–O–Ti bond in the [001] direction due to an electric field $\bar{e}|\mathcal{E}| = 10^{-2}\text{Ry}/a_0$ applied in the direction parallel to the bond. Solid line: WF. Dashed line: NGWF. The corresponding ground state wave functions are displayed in Fig. 8.

character on the top than on the bottom. This feature is captured by both WFs and NGWFs.

The main difference between WFs and NGWFs is the presence of the p_z -like contributions at distant O atoms on the top and bottom of the figures, in the case of orthogonal Wannier functions. The better localization of NGWFs as compared to WFs is also apparent in Fig. 2 which plots the line cuts along rotation symmetry axis of the profiles displayed in Fig. 12a (WF) and Fig. 12c (NGWF). When the electric field is applied in the [001] direction, a charge transfer occurs between these contributions, which can be seen by comparing Fig. 12a and Fig. 12b. As a consequence, a localization region containing at least 3 unit cells is necessary to perform qualitatively accurate calculations with WFs. On the contrary, for non-orthogonal Wannier functions the charge transfer occurs only in the main body of the wave function, contained within the utmost O atoms (comparison of Figs. 12c and 12d). This alleviates the impact of the localization constraint on the accuracy of the calculations employing NGWFs.

V. CONCLUSIONS

We have developed a formalism for calculating the response of an insulator to a static, homogeneous electric field based on an optimization of non-orthogonal generalized Wannier functions. It extends the NV approach to finite electric fields in which orthogonal Wannier functions are used to write a functional for the electric enthalpy of a solid in a uniform electric field. We have implemented this formalism in a fully self-consistent pseudopotential LDA scheme and applied it to representative systems.

This has allowed us to assess the practical usefulness of the method.

The analysis carried out has demonstrated the ability of polarized Wannier functions to highlight the changes of chemical bonding in solids due to applied electric field. As has also been shown, the localized orbitals allow for an intuitive understanding of the effects of the field in terms of displacements of centroids of charge of the wave functions. Therefore a decomposition of the electronic response coming from the individual orbitals is readily available. The main qualitative features are shared be-

tween orthogonal and non-orthogonal orbitals. However our results have clearly demonstrated that the higher localization of non-orthogonal wave functions does not affect the physical results.

As future developments, the proposed method could possibly be extended to use more orbitals than the number of occupied bands. The density kernel matrix would then play the role of generalized occupation numbers¹⁶. The inclusion of extra orbitals would enable long-range charge transfers in the minimization process, irrespective of the extent of the localization regions of the wave functions. This has been shown to decrease the error in the variational estimate of the ground state energy in the context of zero field calculations based on localized Bloch-like orbitals⁴⁹. For the finite field calculations the ability of working with truly localized Wannier-like non-orthogonal orbitals, as in our formulation, is a necessary first step.

ACKNOWLEDGMENTS

This work was supported by SNF Grants No. PP00P2_159314 and 200021_149495.

Appendix A: Use of the Chemical Potential to Ensure the Variational Property of the Minimized Energy Functional

In this Appendix we justify the approach consisting of shifting the eigenspectrum of the Hamiltonian operator, to make its eigenvalues negative. This is done by using the chemical potential parameter μ in the optimization procedure, as introduced in Sec. III. To this end, the minimized energy functional is compared with the exact one and its variational properties are revealed.

The single-particle density matrix written for overlapping orbitals is given by⁵⁰

$$\hat{\rho}[\{\nu\}, \mathbf{S}^{-1}] = 2 \sum_{ab} |\nu_a\rangle (\mathbf{S}^{-1})_{ab} \langle \nu_b|, \quad (\text{A1})$$

where \mathbf{S}^{-1} is the inverse of the overlap matrix \mathbf{S} in Eq. (14), $\mathbf{S}^{-1} \times \mathbf{S} = \mathbf{I}$. For notational simplicity the indexing over cell replicas is dropped in this Appendix.

The exact electronic energy $W[\{\nu\}, \mathbf{S}^{-1}]$, evaluated as the trace of the product of the density matrix in Eq. (A1) and the Hamiltonian operator in Eq. (4), can be written as

$$W[\{\nu\}, \mathbf{S}^{-1}] = 2 \sum_{ab} (\mathbf{S}^{-1})_{ab} \langle \nu_a | \hat{H} | \nu_b \rangle. \quad (\text{A2})$$

Note that Eq. (A2) corresponds to the DFT energy functional written for overlapping orbitals. It is used in large scale electronic structure calculations⁵⁰ and *ab initio* molecular dynamics simulations⁵¹, under zero electric-field conditions.

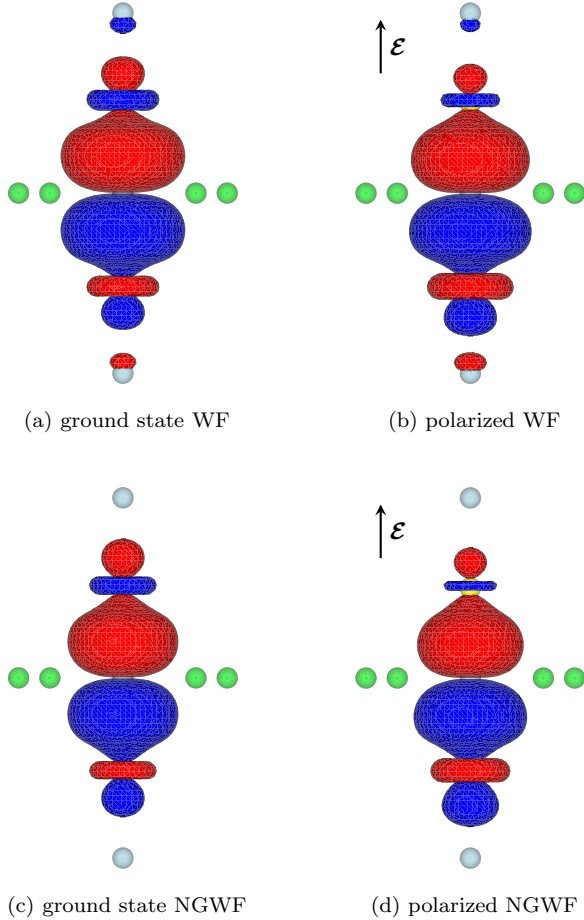


FIG. 12 (Color online). BaTiO₃: Amplitude isosurface plots of oxygen-centered σ wave functions at zero electric field (ground state orbitals) and in presence of macroscopic electric field (polarized orbitals). Isosurfaces at $\pm 2 \times 10^{-3} a_0^{-3/2}$ (red and blue surfaces correspond to positive and negative amplitudes respectively). The orbitals are oriented along O–Ti–O–Ti–O chains in the [001] direction. A O atom is at the center, embedded in a p_z orbital; above and below are Ti atoms (yellow), almost hidden under d_{z^2} orbitals; the two other O atoms (light blue) are visible on top and bottom. The four Ba atoms (light green) neighboring the central oxygen are also shown. The polarized orbitals are induced by the electric field \mathcal{E} along [001] direction as indicated by arrows. Drawings created with VESTA program⁴⁵.

The expression for the electronic enthalpy introduced in Eq. (16) and used in the minimization procedure of Sec. III is restated below

$$W[\{\nu\}, \mathbf{Q}] = 2 \sum_{ab} Q_{ab} \langle \nu_a | \hat{H} | \nu_b \rangle, \quad (\text{A3})$$

where

$$\mathbf{Q} = 2\mathbf{K} - \mathbf{K} \times \mathbf{S} \times \mathbf{K}, \quad (\text{A4})$$

as given in Eq. (13).

This energy functional corresponds to the transformed density operator defined in Eq. (10)

$$\hat{\rho}[\{\nu\}, \mathbf{Q}] = 2 \sum_{ab} |\nu_a\rangle Q_{ab} \langle \nu_b|. \quad (\text{A5})$$

The difference between the approximate and exact energy functionals

$$\Delta W = W[\{\nu\}, \mathbf{Q}] - W[\{\nu\}, \mathbf{S}^{-1}], \quad (\text{A6})$$

can be calculated with the method of Mauri *et al.*⁵². In this approach, the changes in the energy functional are parameterized with respect to a dimensionless parameter λ . The latter varies continuously from zero, which corresponds to $W[\{\nu\}, \mathbf{S}^{-1}]$, to one, which is equivalent to $W[\{\nu\}, \mathbf{Q}]$. Hence, Eq. (A6) can be written as

$$\Delta W = \int_0^1 \frac{\partial W[\{\nu\}, \mathbf{A}(\lambda)]}{\partial \lambda} d\lambda, \quad (\text{A7})$$

where $\mathbf{A}(\lambda) = \lambda \cdot (\mathbf{Q} - \mathbf{S}^{-1}) + \mathbf{S}^{-1}$.

By combining Eqs. (A2) and (A3), Eq. (A7) can be evaluated as

$$\Delta W = \sum_{ab} (\mathbf{Q} - \mathbf{S}^{-1})_{ab} \langle \nu_a | \hat{H} | \nu_b \rangle, \quad (\text{A8})$$

where \hat{H} is the λ -averaged Hamiltonian operator, given by

$$\hat{H} = -\frac{1}{2} \nabla^2 + \hat{V}_{ext} + \int_0^1 \hat{V}_{HXC}(\lambda) d\lambda. \quad (\text{A9})$$

Here, $\hat{V}_{ext} = \hat{V}_{ion} + \mathcal{E} \cdot \mathbf{r}$ and $\hat{V}_{HXC}(\lambda) = \hat{V}_H(\lambda) + \hat{V}_{XC}(\lambda)$, where the Hartree and exchange-correlation potentials are calculated using the charge density $\rho[\{\nu\}, \mathbf{A}(\lambda)]$, when integrating over λ .

By recalling the definition of the \mathbf{Q} matrix, repeated in Eq. (A4), the matrix $(\mathbf{Q} - \mathbf{S}^{-1})$ appearing in Eq. (A8) can be expressed as

$$(\mathbf{Q} - \mathbf{S}^{-1}) = -\mathbf{S}^{-1} \times (\mathbf{I} - \mathbf{S} \times \mathbf{K})^2. \quad (\text{A10})$$

The above form shows that $(\mathbf{Q} - \mathbf{S}^{-1})$ is negative-definite (ND) — it can be seen from Eq. (A10) that it is the negation of a product of two positive-definite (PD) matrices. The \mathbf{S}^{-1} matrix is PD since the overlap matrix \mathbf{S} possesses this property and every PD matrix is

invertible and its inverse is also PD⁵³. The PD property of the second term in Eq. (A10) follows directly from the fact that it is the square of a matrix. A similar line of argument can be used to prove that the $(\mathbf{Q} - \mathbf{S}^{-1})$ matrix is ND too when optimizing the orthogonal Wannier functions with $\mathbf{K} = \mathbf{I}$.

Given a finite basis set, one can choose the μ parameter large enough so that all eigenvalues of the operator

$$\hat{H}(\mu) = \hat{H} - \hat{I}\mu \quad (\text{A11})$$

are negative, $\hat{H}(\mu) \prec 0$. Then, the $(N/2 \times N/2)$ matrix $\langle \nu_a | (\hat{H} - \hat{I}\mu) | \nu_b \rangle$ is also ND. This requirement defines the chemical potential parameter μ .

By substituting Eq. (A11) into Eq. (A8) it can be verified that the eigenspectrum shift of the Hamiltonian ensures that ΔW is non-negative, because it is equal to the trace of a product of two ND matrices. This proves that if μ satisfies $\hat{H}(\mu) \prec 0$, then it holds:

$$W[\{\nu\}, \mathbf{Q}] \geq W[\{\nu\}, \mathbf{S}^{-1}]. \quad (\text{A12})$$

The above inequality gives the desired variational property. It ensures that our variational principle in Eq. (A3) has the exact Kohn-Sham ground-state energy as its absolute minimum. Consequently, no spurious solutions are generated.

The equality in Eq. (A12) holds for each set of $\{\nu\}$, when $\mathbf{K} = \mathbf{S}^{-1}$, as can be seen from Eqs. (A2), (A3), and (A4). In this case $\Delta W = 0$, as is apparent from Eqs. (A8) and (A10). Thus, the auxiliary matrix \mathbf{K} at the minimum becomes a generalized inverse of the overlap matrix of the localized orbitals. The property $\mathbf{K} = \mathbf{S}^{-1}$ results in a weakly idempotent density matrix, $\hat{\rho}^2 = \hat{\rho}$, as can be concluded from Eqs. (A4) and (A5).

Finally, we note that when the functional $W[\{\nu\}, \mathbf{Q}]$ is minimized with respect to $\{\nu\}$, with the density kernel fixed and set to the identity matrix, i.e. $\mathbf{K} \equiv \mathbf{I}$, the equality in Eq. (A12) can be realized by $\mathbf{S} = \mathbf{I}$. This follows from Eqs. (A2), (A3), and (A4), with $\mathbf{Q} = 2\mathbf{I} - \mathbf{S}$. Thus, the optimized orbitals are orthogonal. In this case, the functional in Eq. (A3) corresponds to the one derived by Mauri *et al.*⁵² and Ordejon *et al.*⁵⁴. In our approach, by varying \mathbf{K} , the optimized orbitals are allowed to be non-orthogonal, which improves their localization.

Appendix B: Position Operator in Extended Systems

The position operator in extended systems has been investigated in detail by Resta in Ref. 55. In this Appendix we summarize the main results relevant in the context of finite-field calculations.

Within the Schrödinger representation the result of the position operator, $\hat{\mathbf{r}}$, acting on a wave function, ϕ , equals the coordinate function, \mathbf{r} , multiplied by the wave function, $(\hat{\mathbf{r}}\phi)(\mathbf{r}) = \mathbf{r}\phi(\mathbf{r})$.⁵⁶ This applies only to localized

orbitals which belong to the class of square-integrable wave functions. In the basis of periodic Bloch functions, $\{\psi\}$, this operation becomes ill-defined because of the following argument. The Hilbert space of the single particle wave functions is determined by the condition $\psi(\mathbf{r} + \mathbf{R}) = \psi(\mathbf{r})$, where the lattice vector \mathbf{R} specifies the imposed periodicity. An operator maps any function of the given space into another function belonging to the same space. This cannot be true for the position operator acting on a Bloch wave function, ψ , since

$$\mathbf{r}\psi(\mathbf{r}) \neq (\mathbf{r} + \mathbf{R})\psi(\mathbf{r} + \mathbf{R}). \quad (\text{B1})$$

As can be seen from Eq. (B1) the multiplicative position operator $\hat{\mathbf{r}}$ is not a legitimate operator when periodic boundary conditions are adopted for the Bloch functions, since $\hat{\mathbf{r}}\psi(\mathbf{r})$ is not a periodic function, even if $\psi(\mathbf{r})$ is.

This problem was addressed by Resta⁵⁵ who proposed to define the expectation value of the position operator in periodic systems by using the Berry phase approach, with much of the conceptual work stemming from the ear-

lier development of the modern theory of polarization⁶. One of the most relevant features of this method is that the position operator in an extended quantum system within periodic boundary conditions is no longer a single-particle operator: it acts as a genuine many-body operator on the periodic wave function of N electrons. This renders its implementation particularly challenging.

On the contrary, the position operator can be readily evaluated in the basis of Wannier-like functions. The matrix elements of the position operator in this representation can be calculated directly, using real-space integrals

$$\langle \nu_a^i | \hat{\mathbf{r}} | \nu_b^j \rangle = \int \nu_a^0(\mathbf{r} + \mathbf{R}_i) \nu_b^0(\mathbf{r} + \mathbf{R}_j) \mathbf{r} dV, \quad (\text{B2})$$

where the periodicity relation in Eq. (8) is used to express the remaining orbitals in terms of the electronic degrees of freedom, which are indicated by the superscript 0 and centered in the unit cell containing the origin. In practical calculations the integration takes place over the part of space where the two localized orbitals overlap. Since the wave functions are truncated to finite localization regions this operation is well-defined.

* pawell@iis.ee.ethz.ch

- ¹ P. Lenarczyk and M. Luisier, in *2016 International Conference on Simulation of Semiconductor Processes and Devices (SISPAD)* (2016) pp. 311–314.
- ² R. Resta and D. Vanderbilt, “Theory of polarization: A modern approach,” in *Physics of Ferroelectrics: A Modern Perspective* (Springer Berlin Heidelberg, Berlin, Heidelberg, 2007) pp. 31–68.
- ³ P. Giannozzi, S. de Gironcoli, P. Pavone, and S. Baroni, *Phys. Rev. B* **43**, 7231 (1991).
- ⁴ Z. H. Levine, *Phys. Rev. B* **42**, 3567 (1990).
- ⁵ R. W. Nunes and D. Vanderbilt, *Phys. Rev. Lett.* **73**, 712 (1994).
- ⁶ R. D. King-Smith and D. Vanderbilt, *Phys. Rev. B* **47**, 1651 (1993).
- ⁷ P. Fernández, A. Dal Corso, and A. Baldereschi, *Phys. Rev. B* **58**, R7480 (1998).
- ⁸ P. W. Anderson, *Phys. Rev. Lett.* **21**, 13 (1968).
- ⁹ J. J. Mortensen and M. Parrinello, *J. Phys. Condens. Matter* **13**, 5731 (2001).
- ¹⁰ E. Hernández, M. J. Gillan, and C. M. Goringe, *Phys. Rev. B* **53**, 7147 (1996).
- ¹¹ C.-K. Skylaris, A. A. Mostofi, P. D. Haynes, O. Diéguez, and M. C. Payne, *Phys. Rev. B* **66**, 035119 (2002).
- ¹² N. Troullier and J. L. Martins, *Phys. Rev. B* **43**, 1993 (1991).
- ¹³ W. Kohn and L. J. Sham, *Phys. Rev.* **140**, A1133 (1965).
- ¹⁴ P. Hohenberg and W. Kohn, *Phys. Rev.* **136**, B864 (1964).
- ¹⁵ M. C. Payne, M. P. Teter, D. C. Allan, T. A. Arias, and J. D. Joannopoulos, *Rev. Mod. Phys.* **64**, 1045 (1992).
- ¹⁶ N. Marzari, A. A. Mostofi, J. R. Yates, I. Souza, and D. Vanderbilt, *Rev. Mod. Phys.* **84**, 1419 (2012).
- ¹⁷ W. Hierse and E. B. Stechel, *Phys. Rev. B* **50**, 17811 (1994).
- ¹⁸ E. B. Stechel, A. R. Williams, and P. J. Feibelman, *Phys. Rev. B* **49**, 10088 (1994).

- ¹⁹ R. McWeeny, *Rev. Mod. Phys.* **32**, 335 (1960).
- ²⁰ See G. Galli, *Curr. Opin. Solid State Mater. Sci.* **1**, 864 (1996), and the references therein for details.
- ²¹ J. R. Chelikowsky, “PARSEC quantum mechanics applied to materials,” <http://parsec.ices.utexas.edu/>, accessed: 2018-05-15.
- ²² J. R. Chelikowsky, N. Troullier, and Y. Saad, *Phys. Rev. Lett.* **72**, 1240 (1994).
- ²³ L. Kleinman and D. M. Bylander, *Phys. Rev. Lett.* **48**, 1425 (1982).
- ²⁴ D. M. Ceperley and B. J. Alder, *Phys. Rev. Lett.* **45**, 566 (1980).
- ²⁵ J. P. Perdew and A. Zunger, *Phys. Rev. B* **23**, 5048 (1981).
- ²⁶ E. Polak, *Computational methods in optimization: a unified approach*, Mathematics in science and engineering, Vol. 77 (Academic Press, New York, 1971).
- ²⁷ P. D. Haynes, C.-K. Skylaris, A. A. Mostofi, and M. C. Payne, *J. Phys. Condens. Matter* **20**, 294207 (2008).
- ²⁸ W. H. Press, S. A. Teukolsky, W. T. Vetterling, and B. P. Flannery, *Numerical Recipes 3rd Edition: The Art of Scientific Computing*, 3rd ed. (Cambridge University Press, New York, NY, USA, 2007).
- ²⁹ R. M. Martin, *Electronic Structure: Basic Theory and Practical Methods* (Cambridge University Press, 2004).
- ³⁰ J. D. Cloizeaux, *Phys. Rev.* **135**, A685 (1964).
- ³¹ W. Kohn, *Phys. Rev.* **115**, 809 (1959).
- ³² L. He and D. Vanderbilt, *Phys. Rev. Lett.* **86**, 5341 (2001).
- ³³ G. Nenciu, *Communications in Mathematical Physics* **91**, 81 (1983).
- ³⁴ W. Kohn, *Chemical Physics Letters* **208**, 167 (1993).
- ³⁵ S. Ismail-Beigi and T. A. Arias, *Phys. Rev. Lett.* **82**, 2127 (1999).
- ³⁶ A. M. N. Niklasson, *Phys. Rev. B* **66**, 155115 (2002).
- ³⁷ A. M. N. Niklasson and M. Challacombe, *Phys. Rev. Lett.*

- 92**, 193001 (2004).
- ³⁸ A. M. N. Niklasson, C. J. Tymczak, and M. Challacombe, *The Journal of Chemical Physics* **118**, 8611 (2003).
- ³⁹ A. M. N. Niklasson, V. Weber, and M. Challacombe, *The Journal of Chemical Physics* **123**, 044107 (2005).
- ⁴⁰ X.-P. Li, R. W. Nunes, and D. Vanderbilt, *Phys. Rev. B* **47**, 10891 (1993).
- ⁴¹ R. W. Nunes and D. Vanderbilt, *Phys. Rev. B* **50**, 17611 (1994).
- ⁴² N. Marzari and D. Vanderbilt, *First-Principles Calculations for Ferroelectrics Aip Conference Proceedings*, 146 (1998).
- ⁴³ H. J. Monkhorst and J. D. Pack, *Phys. Rev. B* **13**, 5188 (1976).
- ⁴⁴ See for instance A. Dal Corso, S. Baroni, and R. Resta, *Phys. Rev. B* **49**, 5323 (1994); Z. H. Levine and D. C. Allan, *ibid.* **44**, 12781 (1991), and references therein.
- ⁴⁵ K. Momma and F. Izumi, *J. Appl. Crystallogr.* **44**, 1272 (2011).
- ⁴⁶ See P. H. Ghosez, X. Gonze, and J. P. Michenaud, *Ferroelectrics* **206**, 205 (1998), and references therein.
- ⁴⁷ J. D. Axe, *Phys. Rev.* **157**, 429 (1967).
- ⁴⁸ M. Posternak, R. Resta, and A. Baldereschi, *Phys. Rev. B* **50**, 8911 (1994).
- ⁴⁹ J. Kim, F. Mauri, and G. Galli, *Phys. Rev. B* **52**, 1640 (1995).
- ⁵⁰ G. Galli and M. Parrinello, *Phys. Rev. Lett.* **69**, 3547 (1992).
- ⁵¹ T. A. Arias, M. C. Payne, and J. D. Joannopoulos, *Phys. Rev. Lett.* **69**, 1077 (1992).
- ⁵² F. Mauri, G. Galli, and R. Car, *Phys. Rev. B* **47**, 9973 (1993).
- ⁵³ R. A. Horn and C. R. Johnson, “Positive definite matrices,” in *Matrix Analysis* (Cambridge University Press, 1985) pp. 391–486.
- ⁵⁴ P. Ordejón, D. A. Drabold, M. P. Grumbach, and R. M. Martin, *Phys. Rev. B* **48**, 14646 (1993).
- ⁵⁵ R. Resta, *Phys. Rev. Lett.* **80**, 1800 (1998).
- ⁵⁶ D. J. Griffiths, *Introduction to quantum mechanics*, second edition ed. (Cambridge University Press, Cambridge United Kingdom, 2017).